ORIGINAL PAPER

Hysteresis in Refrigeration

physica status solidi b

www.pss-b.com

Multiferroic and Related Hysteretic Behavior in Ferromagnetic Shape Memory Alloys

Jonathan F. Gebbia, Teresa Castán, Pol Lloveras, Marcel Porta, Avadh Saxena, and Antoni Planes*

We combine a Ginzburg–Landau model for a ferroelastic transition with the theory of micromagnetism to study the magnetostructural behavior leading to multicaloric effects in ferromagnetic shape memory alloys. We analyze the ferroelastic transition under different conditions of temperature, stress and magnetic field and establish the corresponding phase diagram. On the one hand, our results show that the proper combination of both fields may be used to reduce the transition hysteresis and thus improve the reversibility of the related elastocaloric effects, superelasticity and stress-mediated magnetocaloric effects. On the other hand, the stress-free magnetic field-driven and thermally driven magnetostructural evolution provides physical insight into the low-temperature field-induced domain reorientation, from which we derive strategies to modify the operational temperature ranges and thus the corresponding (magnetic) shape-memory effect.

1. Introduction

Technological implementation of functional properties displayed by magnetostructural materials is often hindered by some fundamental drawbacks such as large required fields, cycling fatigue, inappropriate operational ranges, and/or low reversibility due to large hysteresis. Well-known examples are the shape-memory effect and superelasticity, used in sensors, actuators and other technologies,[1,2] and caloric effects, the latter currently attracting great interest due to their potential in more efficient, environmentally friendly solid-state cooling devices.[3,4] At present, most usual methods to overcome the aforementioned obstacles mainly consist of tuning material's properties by means of structural modification at the microscale through doping,[5,6] grain refinement[7–10] and nanocomposite engineering,[11–17] mechanical treatments,[18] mechanical and thermal training,[19] etc. Although these strategies usually involve some degree of serendipity, attempts to systematically implement smart search methods aimed at finding optimal compositions have been recently proposed.[20]

Nevertheless, in some cases alternative solutions could be found by designing smart strategies in terms of applied external fields. A clear example is precisely the case of caloric effects, where the tensor/vector character of the fields allows the possibility of applying a given field in different directions, yielding changes in the caloric performance. For instance, application of a tensile or compressive stress in some elastocaloric materials may change the conventional behavior to the inverse behavior or vice versa.[21] Also, application of a magnetic field along different axes, or even rotating fields may entail a significant enhancement of the caloric effects due to a highly anisotropic entropy change.[22]

Moreover, the possibility of simultaneous application of multiple fields in multiferroic materials has also been shown to improve the caloric performance, such as enhancement of the magnitude of the total caloric response and/or the decrease in the magnitude of the needed applied field,[23] the temperature span of the operational regime,[24] and the reduction of hysteresis,[25] the latter being crucial for an optimal reversibility of the caloric effects upon cycling.[26]

Regarding hysteretic effects, it is worth recalling that the (magnetic) shape memory effect takes place thanks to the low-temperature hysteresis as it originates from the irreversible field-induced domain reorientation. Therefore, it is also interesting to explore how the combination of both magnetic and stress fields may affect the occurrence of this phenomenon.[27]

In this work, we focus on the magnetostructural response of ferromagnetic shape memory alloys at the mesoscale by means of numerical simulations, particularizing on the prototypical Ni_2MnGa Heusler alloy. First, we will focus on the elastocaloric effect associated with the stress-induced ferroelastic transition and the effect of simultaneous application of magnetic and stress fields, aiming in this way at inferring appropriate multiferroic procedures to improve the caloric performance. We will also address the stress-free evolution of the magnetostructure when

J. F. Gebbia, P. Lloveras
Departament de Física, EEBE, Campus Diagonal-Besòs and Barcelona Research Center in Multiscale Science and Engineering, Universitat Politècnica de Catalunya, Eduard Maristany, 10-14, 08019 Barcelona, Catalonia, Spain

T. Castán, M. Porta, A. Planes
Departament de Física de la Matèria Condensada, Facultat de Física, Universitat de Barcelona, Martí i Franquès 1, 08028 Barcelona, Catalonia, Spain
E-mail: antoni.planes@fmc.ub.edu

A. Saxena
Theoretical Division, Los Alamos National Laboratory, Los Alamos, NM 87545, USA

DOI: 10.1002/pssb.201700327

controlling temperature and magnetic field, the latter being at the origin of the ferromagnetic shape memory effect.

The paper is organized as follows: in the next section, we introduce some concepts related to the material and multiferroic features under study. In Section 3, we sketch the theoretical model whereas in Section 4 the phase diagram and the numerical simulations are presented. Section 5 is devoted to the summary and conclusions.

2. Ferromagnetic Shape Memory Ni-Mn-Based Heusler Alloys, Related Caloric Effects and Hysteresis

Heusler alloys include intermetallic alloys of the type X_2YZ that acquire an $L2_1$ structure below a given order–disorder temperature.[28,29] Among them, Ni-Mn-based alloys are particularly interesting due to their magnetic properties and their strong interplay with the underlying crystal lattice.[30] This alloy family is characterized by a ferromagnetic transition at the Curie temperature T_c and a first-order thermoelastic martensitic (i.e., ferroelastic) transition starting at temperature T_M. Depending on the specific composition,[31,32] which involves changes in the third element and/or off-stoichiometric composition and/or doping, T_c and T_M may occur independently at different temperatures ($T_c > T_M$ or conversely) or coupled at the same temperature, $T_M = T_c$, implying that the ferromagnetic transition becomes a first-order one. In addition, when $T_c > T_M$, significant changes in the magnetization may also arise at T_M leading to metamagnetic behavior, with the emergence of, for instance, antiferromagnetic[33] or ferrimagnetic phases.[34]

Interestingly, the coupling between magnetic and structural degrees of freedom always takes place either across the ferroelastic transition due to the above-stated intrinsic changes in the magnetic character correlated with the changes in the crystal symmetries and lattice parameters, or due to a strong magnetocrystalline anisotropy that establishes correlations with the different symmetry-related strain domains (or variants). Such interplays enable in the former case the possibility of driving the ferroelastic transition by means of a magnetic field (i.e., the magnetic superelasticity[35]), whereas in the latter case it is at the origin of the magnetic field-induced reorientation of strain domains (i.e., the ferromagnetic shape memory effect[36]). Here we focus on the Ni_2MnGa Heusler alloy, with its $T_c = 400$ K placed much above its $T_M = 200$ K, and which belongs to the second type of alloys. However, across the ferroelastic transition it undergoes a small change in the magnitude of its magnetic moment, nonetheless keeping its ferromagnetic character. Therefore, Ni_2MnGa permits large elastocaloric (eC) effects and small magnetocaloric (MC) effects across the structural phase transition.[33]

Indeed, Heusler alloys are being investigated for the emergence of large caloric effects associated with their structural transitions. Caloric effects can be defined thermodynamically as the isothermal entropy changes ΔS that occur in physical systems as a response to the application of an external field y (magnetic, electric, mechanical), and can be derived from integration of Maxwell's relations:[Q5]

$$\Delta S(T, y_1 \rightarrow y_2) = \int_{y_1}^{y_2} \left(\frac{\partial X}{\partial T}\right)_y dy, \tag{1}$$

where X is a generalized displacement (magnetization, polarization, strain) and y is its thermodynamically conjugated field. From this expression it is apparent that, in the solid state, the kernel of the integral may become large across first-order phase transitions, and consequently the associated caloric effects will be large too. In multiferroic systems, the dependence of entropy on all generalized displacements X_i involved must be considered. Such a multiferroic thermodynamic framework has been recently formulated.[37] In the case of magnetostructural systems, strain (ε) and magnetization (M) are the relevant generalized displacements that must be taken into account, and stress σ and magnetic field H are their respective conjugated fields.

3. Modeling

In the present study, we use a mesoscopic approach which has been already presented in previous papers.[38,39] To properly account for the multiferroic character of the Ni_2MnGa alloy, the total free energy of the system $\mathcal{F}_T$ must include both the structural and the magnetic degrees of freedom (F_S and F_M, respectively) as well as a magnetostructural coupling term F_{M-S}, which will give rise to the desired cross response of each generalized displacement to the corresponding nonconjugated field. Hence,

$$\mathcal{F}_T = F_S + F_M + F_{M-S}. \tag{2}$$

3.1. Ferroelasticity

It has been suggested that in the case of cubic symmetries, the relevant physical ferroelastic phenomena can be reduced into a two-dimensional subspace.[40,41] The resulting square-to-rectangular transition is described by a Ginzburg–Landau[42] sixth-order polynomial expansion whose order parameter (OP) corresponds to the deviatoric strain $e \equiv e_2 = \frac{1}{2}(\varepsilon_{xx} - \varepsilon_{yy})$, where ε_{ij} are linearized strain tensor components. To ensure lattice integrity, small non-rectangular deformations (bulk $e_1 = \frac{1}{2}(\varepsilon_{xx} + \varepsilon_{yy})$ and shear $e_3 = \varepsilon_{xy}$ strains) are also permitted by including non-OP harmonic terms. The application of an external stress field $\sigma \equiv \sigma_2 = (\sigma_{xx} - \sigma_{yy})$ is taken into account by a linear coupling with the OP. Then,

$$F_S = \int d^2r \left\{ \frac{A_2(T)}{2} e^2(r) + \frac{\beta}{4} e^4(r) + \frac{\gamma}{6} e^6(r) + \frac{\kappa}{2} |\nabla e(r)|^2 + \frac{A_1}{2} e_1^2(r) + \frac{A_3}{2} e_3^2(r) - \sigma e(r) \right\}. \tag{3}$$

The coefficients are related to second and higher order elastic constants. The coefficient of the quadratic term in the OP $A_2(T)$ depends linearly on temperature and includes the effect of quenched disorder through a stochastic variable as detailed in Ref. [43].

3.2. Magnetism

In addition to the local strain $e(r)$, each lattice site also has an associated local magnetization vector $\mathbf{M}(\mathbf{r}) = M_s\mathbf{m}(\mathbf{r})$ (spin) of constant modulus and variable orientation in 3-d, where M_s is the saturation magnetization and $\mathbf{m}$ is the unit magnetization vector. The thermodynamics of the spins is addressed via the micromagnetic theory.[44,45] Accordingly, the micromagnetic free energy F_M is given by

$$F_M = K_1 \int m_x^2(r) m_y^2(r) d^2r + J \int |\nabla \mathbf{m}(\mathbf{r})|^2 d^2r - \mu_0 M_s \int \left(\frac{1}{2}\mathbf{H}_d + \mathbf{H}_{ext}\right) \cdot \mathbf{m}(\mathbf{r}) d^2r. \quad (4)$$

The first term is the magnetocrystalline anisotropy energy that accounts for the coupling between the spins and the underlying undistorted lattice. The sign of the coefficient K_1 determines the easy axis of magnetization, being $m_x = \pm m_y$ for $K_1 < 0$ (as in the case of Fe-Pd) and $m_x = 0, \pm 1$ for $K_1 > 0$, the latter corresponding to the present case for Ni_2MnGa. Notice that while the magnetization is a 3-d vector, the magnetic anisotropy only considers the in-plane components of the magnetization. The second term corresponds to the exchange interaction accounting for the energy cost of spatial variations of the magnetization orientation, with J the exchange stiffness constant. For $J > 0$ the system becomes ferromagnetic, which corresponds to the present case. Since thermal fluctuations are not taken into account, we assume the Curie temperature to be much higher than the ferroelastic transition, as it occurs in Ni_2MnGa and Fe-Pd alloys. The third term includes the magnetostatic energy associated with the demagnetizing field $\mathbf{H}_d$ and the Zeeman energy. The former is responsible for the long-range magnetic interactions that explain the formation of magnetic domains (stripes) within elastic twins. The Zeeman term favors the magnetization to be aligned with an external applied magnetic field $\mathbf{H}_{ext}$.

3.3. Magnetostructural Coupling

As mentioned before, the magnetocrystalline anisotropy term represents the magnetostructural coupling with the lattice when $e = 0$. Thus, in order to take into account changes in the easy magnetization axis when the lattice is distorted, an additional magnetostructural term coupling the magnetic moment to the strain must be included. The lowest order terms allowed by symmetry are[46]

$$F_{M-S} = B_1 \int d^2r \left[m_x^2(\mathbf{r}) + m_y^2(\mathbf{r})\right] e_1(\mathbf{r}) + B_1 \int d^2r \left[m_x^2(\mathbf{r}) - m_y^2(\mathbf{r})\right] e(\mathbf{r}) + B_2 \int d^2r\, m_x(\mathbf{r}) m_y(\mathbf{r}) e_3, \quad (5)$$

where B_1 and B_2 are magnetostriction coefficients. As e_1 and e_3 are expected to be small, it is straightforward to see that the symmetry between the two easy magnetization axes arising at high temperature [(1,0) and (0,1)] will be broken at low temperature, for $e \neq 0$. In turn, this coupling entails that the magnetization will basically remain in plane, with the third component $m_z \simeq 0$. In contrast to experimental observations,[47] our model assumes that the magnetostriction coefficients do not change across the transition. Nevertheless, this is not physically relevant since the strength of the magnetostructural coupling is small in the paraelastic phase due to small strains ($e \simeq 0$) and large in the ferroelastic phase due to large strains ($e \simeq 6\%$).

Despite the fact that the total free energy is a functional of the three strain components e_1, e, and e_3, this dependency can be reduced to a dependency on e only if, on the one hand, the St. Vénant compatibility constraint between e_1, e, and e_3 is taken into account to maintain lattice integrity[48] and, on the other hand, the resulting expression is minimized in terms of the remaining non-OP strain components. With these considerations, the total free energy that can be expressed in terms of the OP strain only (apart from magnetization), whose formulation makes explicit the long-range and anisotropic character of the non-OP contributions, favoring strain modulations along $\langle 11 \rangle$ directions. The particular expressions can be found elsewhere.[39]

3.4. Simulation Details

In order to obtain stable or metastable states under certain conditions of temperature and external fields, we use a relaxation dynamics for the strain[43] and the Landau–Lifshitz–Gilbert equation for the magnetization.[45] The equations presented above are discretized on a 256×256 or 64×64 square mesh, and finite differences and periodic boundary conditions are used. To optimize computation time, the long-range interactions are calculated in reciprocal space using the FFTW code. The values chosen for the parameters are physically consistent with Ni_2MnGa and are shown in the *Appendix* in physical and reduced units. For comparison, they are shown together with a nonexhaustive summary of experimental, calculated, and/or used parameter values in previous studies on the Ni_2MnGa system.

4. Results

Minimization of the free energy functional described above under specific conditions of external fields (magnetic and stress) and temperature determines the equilibrium magnetic and strain field configurations. Nonetheless, the dynamics for both strain and magnetization allows the stabilization of metastable configurations, which entails these states to strongly depend on history. This is indeed observed in ferroic systems, where the specific transformation path is a key factor crucially influencing the final microstructure. Hysteretic phenomena are probably the most prominent example of such behavior.

As mentioned above, hysteresis in ferromagnetic shape memory alloys occurring in relation to the thermal- and field-driven ferroelastic transition is generally rate-independent, indicating an athermal behavior.[49] Our model is consistent with this feature, as time does not play any role in the dynamics used here. Instead, hysteresis takes place mainly due to the

existence of quenched disorder and long-range interactions, which in turn give rise to characteristic power-law avalanche dynamics. This also underlies the hysteretic behavior related to the low-temperature field-induced domain reorientation.

Before performing numerical simulations of the complete magnetostructural model, it is convenient to analyze first the thermodynamic behavior of the homogeneous contributions only, which will help us to understand the interplay between magnetic and structural degrees of freedom. This is accomplished next in Section 4.1. Later, numerical simulations of the complete model are presented, in particular caloric effects associated with the structural transition (Section 4.2) and thermally and field-induced magnetostructural behavior across and below the transition (Section 4.3).

4.1. Homogeneous *T*-σ-*H* Phase Diagram

A detailed study of the model entails the knowledge of the temperature-fields phase diagram. As the phase stability is given by the homogeneous free energy density $f_{\rm hom}$, this analysis can be restricted to such contribution. In particular, $f_{\rm hom}$ is given by the Landau expansion for the OP strain, the magnetocrystalline anisotropy, the magnetostructural coupling and the coupling to the external fields. As the local magnetization is taken to be constant throughout the temperature range of interest ($T_0 << T_c$, where T_0 is the ferroelastic transition temperature) and considering the magnetization to be in plane (i.e., $m_z = 0$), we can use the additional constraint for the magnetization $m_y^2 = 1 - m_x^2$ to write $f_{\rm hom}$ as follows:

$$f_{\rm hom} = \frac{A_2 T}{2} e^2 + \frac{\beta}{4} e^4 + \frac{\gamma}{6} e^6 + K_1 m_x^2 (1 - m_x^2) + B_1 (2m_x^2 - 1) e - \sigma e - \mu_0 M_s H_j m_j, \quad (6)$$

where for the Zeeman energy (last term) we assume an external magnetic field only in $j = x$ or $j = y$ directions for the sake of simplicity. Notice that the above equation contains all the symmetries of the system and from its minimization the homogeneous equilibrium states can be obtained.

4.1.1. Absence of External Magnetic Field

For $H = 0$ the stable solutions of the magnetization are $m_x = 0$, ± 1. Therefore, the equilibrium solutions for the deformation comply with

$$A(T)e + \beta e^3 + \gamma e^5 = \pm B_1 + \sigma. \quad (7)$$

For $\sigma = 0$, the solutions for e are

$$m_x = 0;\ e(T) > 0, \quad (8a)$$

$$m_x = \pm 1;\ e(T) < 0. \quad (8b)$$

This indicates the cross-correlation between magnetization and strain arising from the magnetostructural coupling that becomes specially relevant in the ferroelastic variants, where e is large. It is worth remarking here that the above solutions are degenerate as the sign of $\pm B_1$ changes along with the magnetization. Hence, it does not entail any symmetry breaking in the strain and any of the solutions (8a) or (8b) can occur. Instead, the application of a stress field $\sigma \neq 0$ does break the strain degeneracy as in that case the free energy will be minimized only by the strain e with the same sign as that of σ, which corresponds to only one of the previous solutions (8a) or (8b). Notice that in that case the subsequent symmetry breaking of the magnetization is partial, as only the easy magnetization axis is selected but the two possible 180°-related orientations are still energetically equivalent.

Numerical resolution of Eq. (7) renders the behavior depicted in **Figure 1** for both the temperature-dependent strain and magnetization under constant stress σ. The evolution of the strain (left axis, red and dark green curves for $\sigma \leq 0$ and $\sigma \geq 0$, respectively) exhibits a discontinuity at the first-order ferroelastic transition, from a small paraelastic strain $\pm e_P$ toward a ferroelastic strain $\pm e_F$. Notice that, in agreement with Eq. (8), both $e > 0$ ($m_x = 0$) and $e < 0$ ($m_x = \pm 1$) are equilibrium strains for $\sigma = 0$ whereas $\sigma > 0$ ($\sigma < 0$) renders $e > 0$ ($e < 0$). This is illustrated in the insets that show the homogeneous free energy profile as a function of strain for each stress ($\sigma = 0$, $\sigma > 0$, and $\sigma < 0$) and temperature ($T < T_0$ and $T > T_0$). For $\sigma = 0$ (indicated by the dashed lines), $f_{\rm hom}$ is degenerate[Q6] for $e > 0$ and $e < 0$. Instead, for $\sigma \neq 0$ (continuous lines), this symmetry is broken. At the right hand side of the insets, schematic

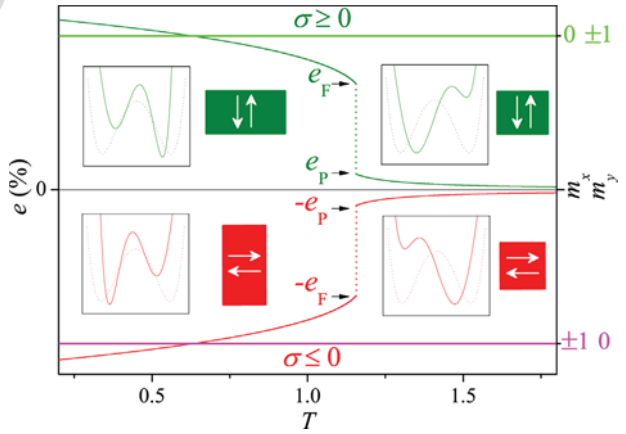

Figure 1. Equilibrium strain e (left axis, red and dark green for $\sigma \leq 0$ and $\sigma \geq 0$, respectively) and magnetization components m_x and m_y (right axis, magenta and light green for $\sigma \leq 0$ and $\sigma \geq 0$, respectively) across the *T*-induced ferroelastic phase transition for a given value of σ as determined from the homogeneous free energy. The equilibrium strains at the transition for the two phases are denoted as $\pm e_P$ (paraelastic strain, which is nearly zero) and $\pm e_F$ (ferroelastic strain), and the snapshots indicate the relative orientation between magnetization and strain variants (i.e., the easy magnetization axis). The insets show the free energy wells as a function of the strain in each stress with different sign (top–bottom) and temperature regime (left–right). Dashed (continuous) lines correspond to $\sigma = 0$ ($\sigma \neq 0$).

COLOR

pictures of equilibrium configurations show the correlated arrangement between strain and the magnetization vector due to the magnetostructural coupling.

The stress-dependent strain, magnetization (m_x component), and temperature in the absence of a magnetic field are shown with black lines in **Figure 2**(a)–(c), respectively. From panel (a), notice that as σ increases, the first-order character of the ferroelastic transition weakens and for a critical stress (indicated by the dotted lines) it finally becomes a second order one with the consequent suppression of hysteresis, in agreement with experimental observations.[50,51] Again, $\sigma < 0$ ($\sigma > 0$) permits both signs for m_x (m_y).

4.1.2. Application of an External Magnetic Field

In contrast to the application of stress, the presence of an external magnetic field does entail the complete symmetry breaking of the magnetization and, consequently, of the strain. Taking advantage of symmetry, from now on we restrict our analysis to the application of a magnetic field in the positive x direction ($h \equiv H/M_s = h_x > 0$) and omit the same analysis for negative h_x and for $h = h_y$ as it would not provide any additional insight. Thus, for a given $h_x > 0$, we can consider three different situations related to an external stress: $\sigma = 0$, $\sigma > 0$, and $\sigma < 0$, as reflected in Figure 2.

i $\sigma = 0$. In this case the homogeneous analysis reveals that the ferroelastic transition is not affected by the magnetic field. This is because the magnetocrystalline anisotropies of the high- and low-temperature phase fulfill a group-subgroup relationship, i.e., the easy axis of any of the ferroelastic variants is also an easy axis of the high-temperature phase. Therefore, when the magnetic field is applied parallel to one of the easy axis of the paraelastic phase, the magnetization direction favored by the magnetic field is compatible with one of the ferroelastic variants (and vice versa) and therefore no ferroelastic distortion needs to take place to accommodate the net magnetization.

ii $\sigma < 0$. In this case the applied stress and the magnetic field select a strain and a magnetization, respectively, that fulfill one of the relations in Eq. (8) [in our particular case, Eq. (8b)], i.e., they favor the same strain variant. In this case, by means of the magnetostructural coupling the stress has already induced a magnetization orientation that minimizes the Zeeman energy, and hence application of an external field does not entail any further change in the magnetization. Consequently, as for the previous case $\sigma = 0$, the transition cannot be induced by the application of a magnetic field.

Summarizing cases (i) and (ii), for $\sigma \leq 0$ the stress-dependent transition strain and temperature are independent of the magnetic field. This is shown in Figure 2(a–c), where all the curves overlap for $\sigma \leq 0$ and therefore only the black line ($h_x = 0$, on top of all of them) is visible. The value of the magnetization is $m_x = 1$ as it aligns parallel to the magnetic field $h_x > 0$. The orange strips denote the phase region belonging to the paraelastic phase for the largest applied magnetic field. Outside this region, the system lies in the ferroelastic phase.

iii $\sigma > 0$. In this case the stress and the magnetic field promote a strain and a magnetization such that they do not fulfill one of the relations in Eq. (8), i.e., they favor opposite variants. This results in a competition between the magnetic field and the stress such that, for a range of stresses, the ferroelastic transition features (strain, magnetization, and temperature) depend on the magnetic field. Thus, it becomes possible to tune the transition by applying a magnetic field which in turn modifies the hysteresis as well as temperature and stress ranges of operation, as it will be shown later in detail.

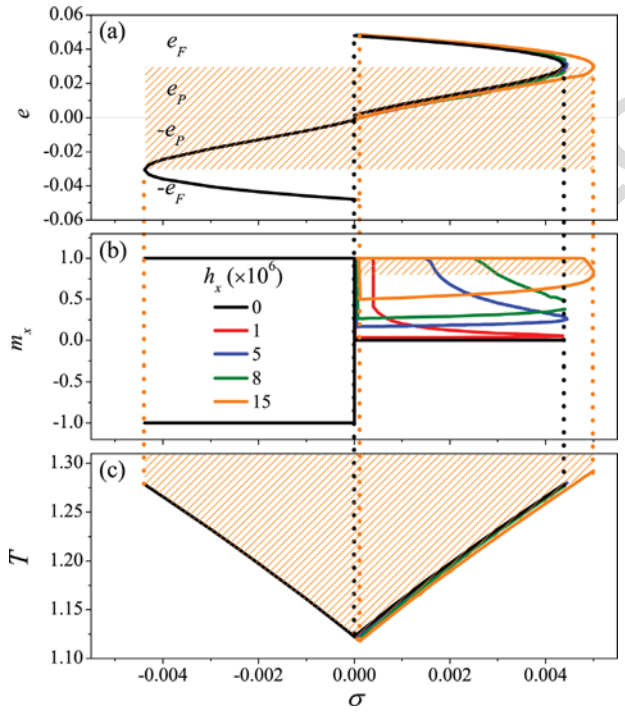

Figure 2. (a) Equilibrium strain, (b) magnetization (x-component), and (c) temperature at the ferroelastic phase transition as a function of the applied stress for different values of the applied magnetic field, as determined from the homogeneous free energy. Dotted lines indicate the critical stress for different values of the applied magnetic field. Legend in (b) is valid for all panels. Orange-stripped regions denote the paraelastic phase in all panels.

Figure 2(a) reveals that for $\sigma > 0$, the critical stress is enhanced when the applied magnetic field increases whereas the equilibrium strain is little affected. Figure 2(b) shows a complex behavior for the magnetization: in the paraelastic phase, since the strain is nearly zero, the magnetostructural coupling plays a minor role compared to the structural contribution, while it becomes more relevant in the ferroelastic phase due to the significant strain values. This entails that the magnetization is more easily aligned with the magnetic field in the paraelastic phase than in the ferroelastic phase. Consequently, m_x will take larger values in the paraelastic phase

[orange curve lying inside the orange-stripped region for the largest magnetic field, as in Figure 2(a)] than in the ferroelastic phase (orange curve lying outside the orange-stripped region for the largest magnetic field).

Obviously, as the magnetic field increases, the magnetization becomes more aligned with the field in both phases. Thus, m_x reaches higher values for $h_x > 0$. For values of the magnetic field above a given threshold, the strain and the magnetization decouple such that the latter is no longer oriented along the easy magnetocrystalline axis but is ruled by the magnetic field only.

As the scale in Figure 2(c) does not provide a clear plot of the magnetic field dependence of the transition temperature, in **Figure 3**(a) we show an enlargement of the T–σ phase diagram for different values of h_x around $\sigma = 0$. Figure 3(c) shows the T–h_x phase diagram under different values of σ, whereas Figure 3(b) and (d) shows the corresponding slopes, $dT/d\sigma$ as a function of the magnetic field and conversely, dT/dh_x as a function of h_x.

4.2. Caloric Effects

The nonhomogeneous contributions add three essential ingredients to the behavior of ferromagnetic shape memory alloys: long-range interactions, interfacial energy, and disorder. As long as these features play a role in determining a specific transformation path, they have to be included to realistically reproduce the hysteretic transition behavior, which in turn is crucial to determine the range and magnitude of the reversible caloric effects. Therefore a faithful modeling of caloric effects requires carrying out numerical simulations of the full model.

Before presenting the numerical results, it is worth pointing out the following consideration: large entropy changes arise due to significant strain changes across the first order phase transition between the paraelastic and the ferroelastic phases. On the other hand, during a low-temperature field-induced domain reorientation process there is also a significant macroscopic change in the strain and magnetization such that this should lead to eC and MC effects. However, as the entropy difference between both initial and end states (multidomain and single domain ferroelastic configurations, respectively) is nearly zero, the eC and MC effects are expected to be negligible.[29,52] Moreover, the field-induced domain reorientation is completely nonreversible as it will completely disappear when the field is removed for the first time. Then, to avoid such effects, we have checked that all initial configurations for the loading processes belong to the square phase.

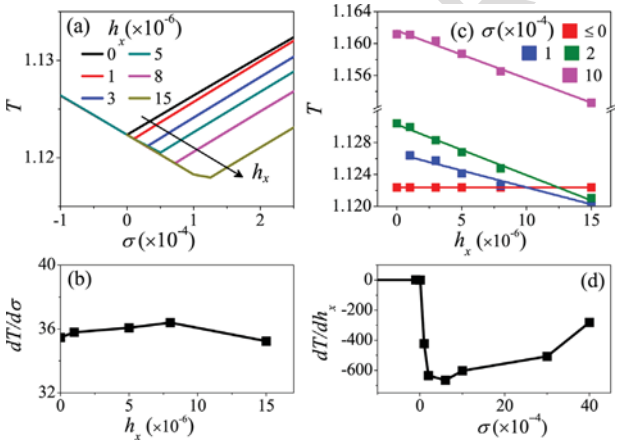

Figure 3. (a) Transition temperature as a function of the applied stress for different values of the applied magnetic field [enlargement of Figure 2(c)]. (b) Transition temperature as a function of the applied magnetic field for different values of the stress. (c) Slope $dT/d\sigma$ as a function of the applied magnetic field and (d) slope of dT/dH as a function of the applied stress.

COLOR

4.2.1. Elastocaloric Effects

We first focus on the eC effects obtained when driving the transition by isothermally applying an increasing external stress field σ in the absence of a magnetic field. From a complete set of isothermal strain–stress curves [shown in Figure4(a)], the eC effect can be computed by integration of the Maxwell relation as follows[53,54]:

$$\Delta S[T, H, 0 \to \sigma] = \int_0^{\sigma} \left(\frac{\partial \varepsilon}{\partial T}\right)_H d\sigma \simeq \frac{1}{\Delta T}\int_0^{\sigma} \{e(T + \Delta T, \sigma, H) - e(T, \sigma, H)\} d\sigma. \quad (9)$$

Results are shown in **Figure 4**(c). The negative sign for ΔS confirms the conventional character of the eC effects, as anticipated from the positive slope in the σ–T diagram [see Figure 2(c)].

To obtain the reversible eC effects, hysteresis must be taken into account, which requires driving the backward isothermal transition by decreasing the applied stress. The corresponding isothermal strain–stress curves upon unloading are shown in Figure 4(b) and the resulting eC effects computed from Eq. (9) are shown in Figure 4(d). An example of a pair of loading/unloading stress–strain curves corresponding to the same temperature have been displayed in Figure 4(a and b) with red thick curves to highlight the hysteresis between the transition stress in both cases. Note that Figure 4(a and b) represents superelastic behavior as large strains are reached nonlinearly by a small stress change driving the transition.

The temperature dependence of the transition stress for loading and unloading processes is displayed in Figure 4(e), showing a decreasing hysteresis with increasing temperature that finally disappears at a critical stress. This is consistent with the previously analyzed phase diagram showing a weakening of the first order character of the transition that finally becomes a continuous second order transition, as observed in experiments.[50,51] The black line in Figure 4(e) corresponds to the homogeneous equilibrium transition stress.

The hysteresis results in different temperature regimes for the corresponding eC effects, as it can be seen by comparing

COLOR

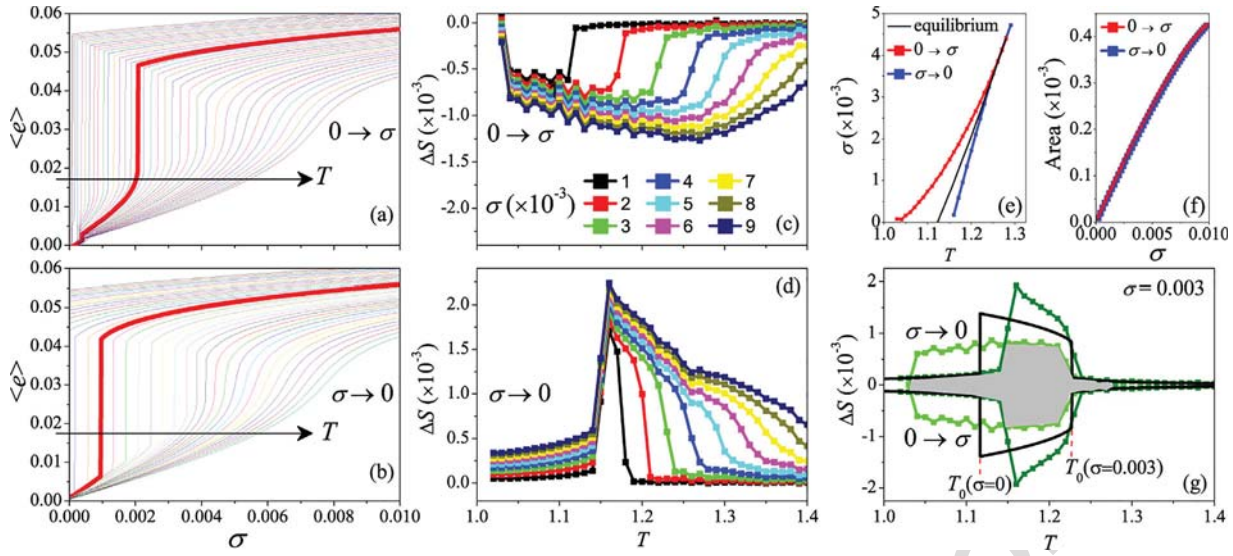

Figure 4. Stress–strain curves in the absence of magnetic field upon (a) loading and (b) unloading. An isothermal loading–unloading cycle is highlighted with a thicker red line to clearly show the stress-induced ferroelastic forward and backward transitions and the corresponding hysteresis. Elastocaloric effects obtained upon (c) loading [as derived from (a)] and (d) unloading [as derived from (b)], by using Eq. (9). (e) Metastable transition stress as a function of temperature upon loading (in red) and unloading (in blue) as derived from panels (a) and (b), respectively, and equilibrium transition stress (black) as derived from the homogeneous phase diagram. (f) Area below the entropy change as derived from (c) (in red) and from (d) (in blue). (g) Reversible entropy change for $\sigma = 0.003$ as derived from the overlap between the corresponding loading and unloading curves. Black lines indicate reversible entropy changes derived from the Landau free energy.

Figure 4(c and d). In particular, the eC peaks are larger when removing stress whereas the temperature range is wider when applying stress. However, for a given applied stress comprising the full transition, the total area below the eC curve must be the same for the loading and unloading processes as the entropy change is the same [which is confirmed in Figure 4(f)]. Reversible eC effects can be determined from the overlap between the eC obtained by loading and unloading processes.[26] An example ($\sigma = 0.003$) is shown in Figure 4(g), where the shaded area indicates the reversible eC effects. It becomes clear how the hysteresis decreases the eC effects that can be implemented in a cooling device using loading–unloading cycles. On the other hand, the small (reversible) contribution outside the transition comes from the temperature-dependent elastic strain of both phases. The black line indicates the eC as computed from the equilibrium homogeneous Landau free energy.

4.2.2. Magnetocaloric and Multicaloric Behavior

We now proceed to apply a constant magnetic field while driving the transition by stress. **Figure 5** shows the dependence of the strain (left axis, continuous line) and the magnetization (right axis, dashed lines) on the applied stress, in the absence of a magnetic field (red lines) and under the application of a magnetic field $h_x = 0.001$ (blue lines). Consistent with case (iii) analyzed in Section 4.1.2, the application of h_x shifts the transition to higher stresses as indicated by the shift of the large increase in the strain. In the absence of the magnetic field (or $h_y \neq 0$), $m_x = 0$ throughout the stress range (red dashed curve), consistent with the sign of e according to the magnetostructural coupling [see Eq. (8)]. Instead, when a magnetic field h_x is applied (blue-dashed curve), the magnetic field and the magnetostructural coupling are in competition. In the paraelastic phase, the magnetization is aligned with the field ($m_x = 1$) because the magnetostructural coupling is small. In contrast, in the ferroelastic phase the magnetostructural coupling becomes large so that it imposes its preferred orientation for the

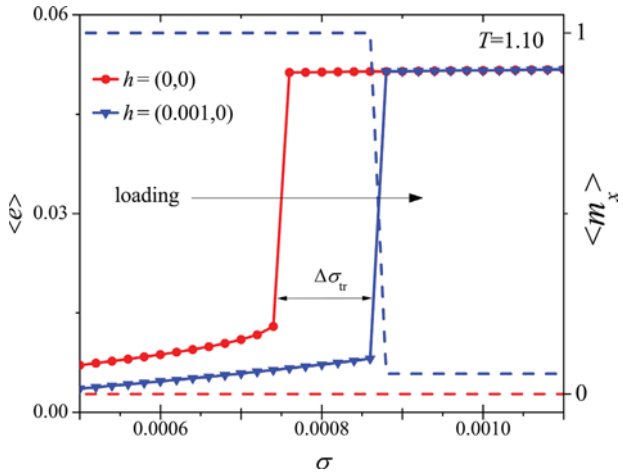

Figure 5. Strain (left axis, continuous lines) and magnetization (right axis, dashed lines) as a function of the stress close to the transition in the absence of a magnetic field (in red) and under $h_x > 0$ (in blue). $\Delta\sigma_{tr}$ indicates the change in the transition stress.

COLOR

magnetization (i.e., $m_x = 0$), despite being unfavorable for the Zeeman energy.

Although our results only report a stress-driven transition (i.e., eC effects), MC effects can be conceived in our model when the transition is induced by an applied magnetic field. In contrast to eC effects, the negative sign of dT/dH [see Figure 3(d)] indicates that MC effects should be of inverse type. It is worth recalling here that this behavior will occur only when a (relatively small) stress field is also applied. In fact, for a large applied stress, the strain will be completely decoupled from the magnetization so that dT/dH will vanish again, as anticipated from the stress dependence of dT/dH [see Figure 3(d)], whose absolute value decreases and tends to zero for large values of stress. Notice that in Ni_2MnGa the magnetic moment changes slightly at the transition, which gives rise to a conventional contribution to the MC effect.[55] As the magnetic moment is assumed to be constant in our model, this contribution cannot be reproduced.

Interestingly, the multiferroic behavior can be used to tune the eC performance. In particular, our results indicate that reversibility of eC effects can be improved by applying (or increasing) a magnetic field during the unloading process with respect to the loading process. Alternatively, hysteresis reduction in MC effects would need the opposite strategy, i.e., applying (or increasing) a constant stress field when driving the transition by means of the magnetic field and/or removing the stress when driving the reverse transition upon decreasing the magnetic field. On the other hand, in addition to hysteresis reduction, temperature range for eC effects can be decreased by applying a constant magnetic field throughout the caloric cycle. Also, MC effects could be shifted to higher temperatures by applying a constant stress.

4.3. Domain Reorientation Under Magnetic Field

4.3.1. Field-Driven Domain Reorientation

In this section we study the isothermal magnetic field-induced ferroelastic domain switching. **Figure 6** displays the evolution of the strain (left axis, in blue) and the magnetization (right axis, in red) when the magnetic field is increased within the ferroelastic phase at constant temperature. The snapshots are simulated magnetic configurations at different steps of the process, from which the structural configuration can be derived by considering the symmetries of the multiferroic coupling [see Eq. (8)]. The gray tone stands for the orientation of the magnetization at each lattice site, as indicated by the illustrative arrows depicted on the snapshots. The initial configuration (i) exhibits a typical magnetostructural microstructure[56]: the strain configuration consists of diagonal twin boundaries separating strain domains of alternating rectangular variants whereas the magnetization exhibits two types of domain walls. On the one hand, within each ferroelastic domain the magnetization is arranged in stripes with 180° domain walls due to a balance between the exchange interaction and the demagnetizing field. The particular orientation is determined by the magnetostructural coupling with each variant. Precisely, the cooperation between the demagnetizing field and the magnetostructural coupling yields 90° domain walls along the twin boundaries.

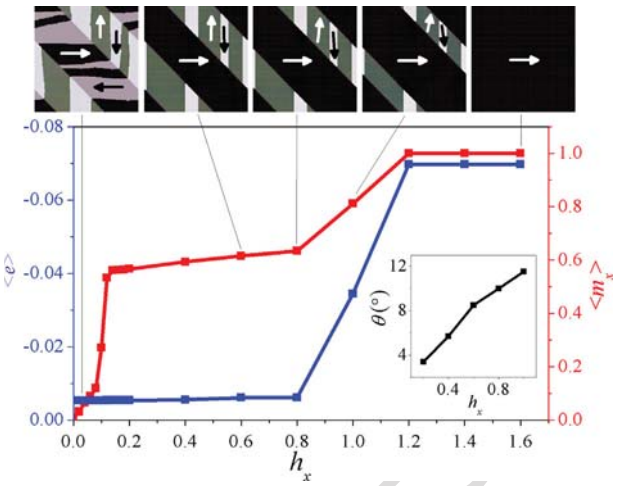

Figure 6. Evolution of the average magnetization and strain as a function of the increasing magnetic field. Snapshots represent magnetic configurations at selected field values as indicated by the thin black lines. The inset shows the evolution of the average angle of magnetization vector with respect to the vertical inside the variants with $e > 0$.

The evolution of magnetization exhibits a large and sharp increase for low values of h_x (i→ii) which is explained as follows: as is evident from Eq. (8), the magnetic field favors one of the two elastic variants through the magnetostructural coupling. Accordingly, the magnetization is first reoriented inside the strain domains favored by the magnetic field, by a 180° switching (from $m_x = -1$ to $m_x = 1$, with local strain e unchanged), as the Zeeman energy only has to overcome the magnetostatic energy. Therefore, the corresponding magnetic stripes are removed there. Instead, the magnetization inside the elastic domains unfavored by the magnetic field offers higher resistance to a 90° switching because this reorientation entails also the reorientation of the corresponding elastic domains (from $m_x = 0$ and $e = -e_F$ to $m_x = 1$ and $e = e_F$). Hence, the magnetic field required for such a process is higher and the magnetic stripes are maintained in the these domains (ii).

Indeed, when h_x is further increased (ii→iv), the width of the magnetic stripes remains essentially constant but the width of the corresponding strain variant is decreased as a consequence of the twin boundary motion that occurs due to the local strain variant reorientation at the twin boundary. This results in a gradual increase in the average strain. Also, the magnetization vectors slightly rotate inside the stripes, acquiring a nonzero m_x component aligned with the field, as it is indicated by the deviation angle from the vertical direction shown in the inset. Above a certain field threshold, the complete strain domain reorientation is accomplished leading to a single strain domain and the spins fully aligned with the field (v). This process is in excellent agreement step by step with experimental observations,[57] and is at the origin of the magnetic shape memory effect (MSME). It is worth noting here that as the domain reorientation can be induced by both the stress and the magnetic field, the simultaneous application of both fields should decrease their magnitude for the MSME.

4.3.2. Thermally Driven Domain Reorientation Under Magnetic Field

For the sake of completeness, it is useful to analyze the evolution of the magnetization across the temperature-induced ferroelastic transition under the application of a constant magnetic field, as displayed in **Figure 7**. The snapshots show magnetic configurations at low and high temperatures for different values of the applied field. If we first consider the case $h_x = 0$, the magnetization is nearly zero both at low (i) and high temperatures (iv). This occurs because of the existence of magnetic domains so that the average magnetization vanishes. This behavior is maintained for low values of the applied magnetic field. When increasing the magnetic field, however, there is an increase of the magnetization at high temperatures as the paraelastic phase is easily magnetized because of the small strength of the magnetostructural coupling (iii). Instead, the coupling becomes stronger in the ferroelastic phase, offering resistance to the reorientation of magnetization in the direction of the magnetic field. Notice that the configurations in the ferroelastic phase for $h_x = 0$ (i) and for $h_x > 0$ (ii) are the same configurations (i) and (ii) shown in Figure 6 as they correspond to the same conditions.

Also, when considering the temperature, the energy required for the domain reorientation (and consequently for the associated switching of magnetization) decreases when the transition is approached and, thus, the average magnetization increases as well. For large magnetic fields, the average magnetization is constant throughout the temperature range. This is fully consistent with experimental observations.[33]

In **Figure 8**(a) temperature-dependent magnetization curves for a full set of magnetic field values is shown, along with the simultaneous monitoring of strain [Figure 8(b)], that confirms the variant switching in the ferroelastic phase driven by magnetic field. Instead, the behavior at and above the transition is almost independent of the magnetic field, indicating that the stress-free transition cannot be induced by the magnetic field, in agreement with the phase diagram analyzed previously.

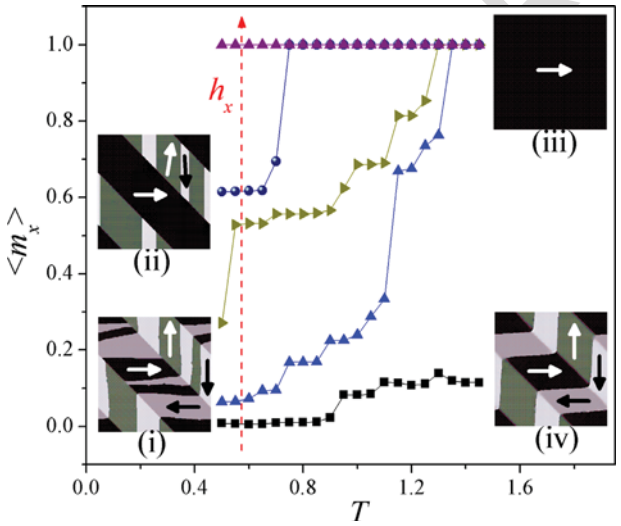

Figure 7. Temperature-dependent magnetization under different applied magnetic fields. Snapshots (i–iv) represent the corresponding magnetic configurations at the lowest and highest temperatures and at zero and nonzero applied fields. The red-dashed arrow indicates the direction of increasing the applied magnetic field.

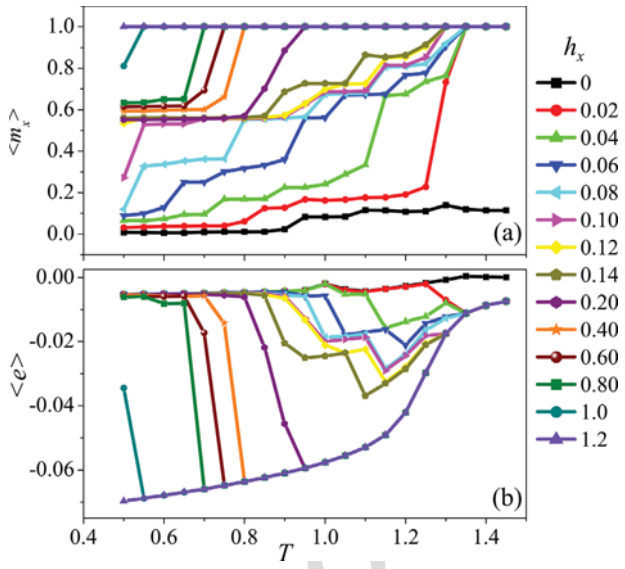

Figure 8. Temperature-dependent magnetization (a) and strain (b) under different applied magnetic fields.

5. Summary and Conclusions

We have studied the multiferroic and hysteretic behavior associated with the ferroelastic transition in ferromagnetic shape memory alloys, focusing on the prototypical Ni_2MnGa Heusler alloy. For this purpose, we have used a magnetostructural model that combines an extended Ginzburg–Landau-based ferroelastic free energy with micromagnetism as well as a magnetostructural coupling enabling a multiferroic cross response. On the one hand, our results predict that the stress-induced transition leads to large elastocaloric effects that in turn can be tuned by appropriate application of a magnetic field. In particular this feature can be used to reduce the transition hysteresis, which entails the enhancement of the reversibility of the associated caloric effects and superelasticity. The corresponding temperature and stress ranges can be modified as well.

On the other hand, our results reproduce both field- and temperature-induced magnetic domain wall dynamics in excellent agreement with experiments. In addition, we have found that ferroelastic domains can be reoriented at low temperature by either stress and/or, more interestingly, magnetic field. This behavior allows to design strategies based on the simultaneous application of both fields to reduce their magnitude required for domain switching and modifying the operational ranges of the subsequent (magnetic) shape memory effect.

Appendix

Parameter values for Ni_2MnGa (Table A1)

Table A1. Nonexhaustive[Q7] summary of parameter values for Ni_2MnGa alloy from literature, either from experiments (Exp) o[Q8] modeling.

			Structural						Magnetic			Magnetostructural	
Ref. (exp/ calc/chosen)	Composition	Unit cell length Å	T_0 (K)	e_F %	A_1 (N m^{-2})	A_2 (N m^{-2})	A_3 (N m^{-2})	κ (N)	M_s (A m^{-1})	K_1 (N m^{-2})	J (N)	B_1 (N m^{-2})	B_2 (N m^{-2})
[58] Exp	Ni_2MnGa	5.825	202						$7.8 \cdot 10^5$				
[36] Exp	Ni_2MnGa	5.822	276	6.56					$3.8 \cdot 10^4$	$[2.7, 11.7] \cdot 10^4$			
[59] Exp	Ni_2MnGa				$2.95 \cdot 10^{11}$	$9 \cdot 10^9$	$4.03 \cdot 10^{11}$						
[60] Exp	$\sim Ni_2MnGa$		175		$2.40 \cdot 10^{11}$	$32 \cdot 10^9$	$4.08 \cdot 10^{11}$						
[61] Exp	$Ni_{54.4}Mn_{21.4}Ga_{24.2}$		377						$1.27 \cdot 10^5$	$8 \cdot 10^5$			
[47] Exp	$Ni_{51.3}Mn_{24.0}Ga_{24.7}$		263	4.3					$6.015 \cdot 10^5$	$[2.7 \cdot 10^3, 2.45 \cdot 10^5]$		$[2, 3] \cdot 10^6$	$\sim[10^5, 10^6]$
[62] Exp	$Ni_{47.4}Mn_{32.1}Ga_{20.5}$		318	6					$4.9 \cdot 10^5$	$1.5 \cdot 10^5$			
[63] Exp	$Ni_{49.75}Mn_{28.5}Ga_{21.75}$	5.84	300	5.4									
[64] Exp/calc					$3.12 \cdot 10^{11}$	$8 \cdot 10^9$	$1.72 \cdot 10^{11}$						
[42] Calc	Ni_2MnGa		200							$\sim 10^5$		$\sim 10^6$	
[65] Calc												$2.1 \cdot 10^9$	
[66] Calc	Ni_2MnGa				$3.15 \cdot 10^{11}$	$11 \cdot 10^9$	$4.28 \cdot 10^{11}$						
[67] Chosen									$3.7 \cdot 10^4$	$2 \cdot 10^5$	$2 \cdot 10^{-11}$		
[68] Chosen				6.1				$1.7 \cdot 10^{-10}$		$1.8 \cdot 10^5$			
[69] Chosen											$2 \cdot 10^{-11}$		
[70] Calc	$Fe_{70}Pd_{30}$							$3.5306 \cdot 10^{-9}$					
This work		5.92	263.15	5.5	$3.12 \cdot 10^{11}$	$8 \cdot 10^9$	$1.72 \cdot 10^{11}$	$1.89 \cdot 10^{-8}$	$6.015 \cdot 10^5$	$2.7 \cdot [10^3, 10^6]$	$[1.77 \cdot 10^{-12}, 1.41 \cdot 10^{-13}]$	$6.46 \cdot [10^7, 10^8]$	$4.98 \cdot 10^5$
This work		1.9417	1	5.5	1.4820	10	0.8170	1	1	$1.28 \cdot [10^{-8}, 10^{-5}]$	$[5 \cdot 10^{-4}, 4 \cdot 10^{-5}]$	$3.076 \cdot [10^{-4}, 10^{-3}]$	$2.451 \cdot 10^{-6}$
(model units)		u.l.	u.T.		(u.f.) (u.l.)$^{-2}$	(u.f.) (u.l.)$^{-2}$	(u.f.) (u.l.)$^{-2}$	(u.f.)	(u.i.) (u.l.)$^{-1}$	(u.f.) (u.l.)$^{-2}$	(u.f.)	(u.f.) (u.l.)$^{-2}$	(u.f.) (u.l.)$^{-2}$

In the latter case, values can be either derived as theoretical outputs (calc) or chosen for simulations (chosen). Symbols refer to the following parameters: T_0, ferroelastic transition temperature; e_F, equilibrium strain in the ferroelastic phase; A_1, bulk modulus; A_2, deviatoric elastic constant; A_3, shear elastic constant; κ, Ginzburg coefficient; M_s, saturation magnetization; K_1, magnetocrystalline anisotropy; J, exchange stiffness constant; B_1 and B_1, magnetoelastic coefficients. Values in brackets give a range of values reported or used. The value for κ from Ref. [70] corresponds to Fe-Pd alloy and has been included due to the lack of data and taking into account that it maintains consistent behavior with Ni_2MnGa alloy. Two last rows correspond to those values used in the present work for comparison, both in S.I. and model units as indicated [(u.l.), (u.f.), (u.T.), and (u.i.) stand for units of length, force, temperature, and current intensity, respectively].

Strictly, our parameter T_0 indicates the low-temperature limit of the high temperature phase. The value for our parameter A_2 is calculated at 273 K and according to Landau theory it is assumed to vary linearly with temperature as $A_2 = \alpha_T[T - T_0 + \eta(\xi, \psi)]$, being $\alpha_T = 8 \cdot 10^8\,\mathrm{N\,K^{-1}\,m^{-2}} = 1$ (u.f.)(u.l.)$^{-2}$(u.T.)$^{-1}$ and $\eta(\xi, , \psi)$ a random variable Gaussian distributed and exponentially correlated accounting for disorder. The values for disorder parameters, $\psi = 26.3 \cdot [10^{-6}, 1]\,\mathrm{K} = 10^{-7}, 10^{-1}$ (u.T.) and $\xi = [3, 6] \cdot 10^{-9}\,\mathrm{m} = [10, 20]$ (u.l.), are not included in the table because they have not a direct counterpart in experimental outputs and they are physically irrelevant for the purposes of the present work. More details can be found in Ref. [43]. From T_c, α_T and e_F, the 4th- and 6th-order Landau coefficients can be calculated, rendering $\beta = -4.292 \cdot 10^{16}\,\mathrm{N\,m^{-2}} = 199.03$ (u.f.)(u.l.)$^{-2}$ and $\gamma = 10^{16}\,\mathrm{N\,m^{-2}} = 6.4 \cdot 10^4$ (u.f.)(u.l.)$^{-2}$ in S.I. and model units respectively. Differences in values between references such as transition temperatures or saturation magnetization may occur due to off-stoichiometry, different measurement temperatures (due to possible temperature dependence of the parameters) and/or measurement methods, single or polycristalline samples, etc. Our values are chosen such that they are *physically consistent* with the behavior of Ni_2MnGa. This means that (i) the ferroelastic transition occurs within the ferromagnetic phase ($T_t < T_C$); (ii) the system is ferromagnetically hard (large magnetocrystalline anistropy K_1 and magnetoelastic coupling parameters B_1 and B_2); and (iii) the easy magnetization axes of the high temperature phase are any of the cubic axes and that of the low-temperature cell is the c-axis ($K_1 > 0$).

Acknowledgements

This work was supported by CICyT (Spain), Projects nos. MAT2016-75823-R and FIS2014-54734-P, by DGU (Catalonia), Project no. 2014SGR00581, and by the U.S. Department of Energy.

Conflict of Interest

The authors declare no conflict of interest.

Keywords

domain reorientation, ferromagnetic shape memory alloys, hysteresis, magnetic field, magnetostructure, multicaloric effects, stress

Received: July 1, 2017
Revised: July 26, 2017
Published online:

[1] K. Otsuka, C. M. Wayman, *Shape Memory Materials*. Cambridge University Press, Cambridge, UK **1998**.
[2] A. Planes, L. Mañosa, A. Saxena, *Magnetism and Structure in Functional Materials*. Springer, Berlin **2005**.
[3] X. Moya, S. Kar-Narayan, N. D. Mathur, *Nature Mater.* **2014**, *13*, 439.
[4] L. Mañosa, A. Planes, *Adv. Mater.* **2017**, *29*, 1603607.
[5] V. Provenzano, A. J. Shapiro, R. D. Shull, *Nature* **2004**, *429*, 853.
[6] J. Cui, Y. S. Chu, O. O. Famodu, Y. Furuya, J. Hattrick-Simpers, R. D. James, A. Ludwig, S. Thienhaus, M. Wuttig, Z. Zhang, I. Takeuchi, *Nature Mater.* **2006**, *5*, 286.
[7] R. Day, M. Fuller, V. A. Schmidt, *Phys. Earth Planet. Inter.* **1977**, *13*, 260.
[8] H. Kwun, G. L. Burkhardt, *J. Appl. Phys.* **1987**, *61*, 1576.
[9] L. E. Hueso, J. Rivas, *J. Appl. Phys.* **1999**, *86*, 3881.
[10] Z. Zhao, V. Buscaglia, M. Viviani, M. T. Buscaglia, L. Mitoseriu, A. Testino, M. Nygren, M. Johnsson, P. Nanni, *Phys. Rev. B* **2004**, *70*, 024107.
[11] J. P. Liu, R. Skomski, *J. Appl. Phys.* **2000**, *87*, 6740.
[12] H. Zheng, J. Wang, S. E. Lofland, Z. Ma, L. Mohaddes-Ardabili, T. Zhao, L. Salamanca-Riba, S. R. Shinde, S. B. Ogale, F. Bai, D. Viehland, Y. Jia, D. G. Schlom, M. Wuttig, A. Roytburd, R. Ramesh, *Science* **2004**, *303*, 661.
[13] M. Murakami, S. Fujino, S.-H. Lim, L. G. Salamanca-Riba, M. Wuttig, I. Takeuchi, *Appl. Phys. Lett.* **2006**, *88*, 112505.
[14] S. J. Kernion, P. R. Ohodnicki, Jr., J. Grossmann, A. Leary, S. Shen, V. Keylin, J. F. Huth, J. Horwath, M. S. Lucas, M. E. McHenry, *Appl. Phys. Lett.* **2012**, *101*, 102408.
[15] A. Chen, Z. Bi, Q. Jia, J. L. MacManus-Driscoll, H. Wang, *Acta Mater.* **2013**, *61*, 2783.
[16] S. Hao, L. Cui, D. Jiang, X. Han, Y. Ren, J. Jiang, Y. Liu, Z. Liu, S. Mao, Y. Wang, Y. Lin, X. REn, X. Ding, S. Wang, C. Yu, X. Shi, M. Du, F. Yang, Y. Zheng, Z. Zhang, X. Li, D. E. Brown, J. Li, *Science* **2013**, *339*, 1191.
[17] H. Tang, Y. Lin, H. A. Sodano, *Adv. Energy Mater.* **2012**, *2*, 469.
[18] T. Saito, T. Furuta, J.-H. Hwang, S. Kuramoto, K. Nishino, N. Suzuki, R. Chen, A. Yamada, K. Ito, Y. Seno, T. Nonaka, H. Ikehata, N. Nagasako, Ch. Iwamoto, Y. Ikuhara, T. Sakuma, *Science* **2003**, *300*, 464.
[19] P. G. Wolynes, V. Lubchenko, *Structural Glasses and Supercooled Liquids: Theory, Experiment and Applications*. Wiley, New Jersey, USA **2012**.
[20] D. Xue, P. V. Balachandran, J. Hogden, J. Theiler, D. Xue, T. Lookman, *Nature Comm.* **2016**, *7*, 11241.
[21] Y. Liu, I. C. Infante, X. Lou, L. Bellaiche, J. F. Scott, B. Dkhil, *Adv. Mater.* **2014**, *26*, 6132.
[22] M. Balli, S. Jandl, P. Fournier, D. Z. Dimitrov, *Appl. Phys. Lett.* **2016**, *108*, 102401.
[23] L. Morellón, et al. *Phys.*[Q9] *Rev. Lett.* **2004**, *93*, 137201.
[24] Y. Sun, et al. *Appl. Phys. Lett.* **2006**, *89*, 172513.
[25] J. Liu, T. Gottschall, K. P. Skokov, J. D. Moore, O. Gutfleisch, *Nature Mater.* **2012**, *11*, 620.
[26] B. Emre, S. Yüce, E. Stern-Taulats, A. Planes, S. Fabbrici, F. Albertini, L. Mañosa, *J. Appl. Phys.* **2013**, *113*, 213905.
[27] A. A. Likhachev, A. Sozinov, K. Ullakko, Proc. SPIE 4333, Smart Structures and Materials 2001: Active Materials: Behavior and Mechanics, 197.
[28] A. J. Bradley, J. W. Rodgers, *Proc. R. Soc. London* **1934**, *A144*, 340.
[29] A. Planes, L. Mañosa, X. Moya, J. Marcos, M. Acet, T. Krenke, S. Aksoy, E. Wassermann, *Adv. Mat. Res.* **2008**, *52*, 221.
[30] G.-H. Yu, Y.-L. Xu, Z.-H. Liu, H.-M. Qiu, Z.-Y. Zhu, X.-P. Huang, L.-Q. Pan, *Rare Met.* **2015**, *34*, 527.
[31] A. Planes, *Physics* **2010**, *3*, 36.
[32] E. Stern-Taulats, A. Planes, P. Lloveras, M. Barrio, J.-Ll. Tamarit, S. Pramanick, S. Majumdar, S. Yüce, B. Emre, C. Frontera, L. Mañosa, *Acta Mater.* **2015**, *96*, 324.
[33] A. Planes, L. Mañosa, M. Acet, *J. Phys. Condens. Matter* **2009**, *21*, 233201.
[34] L. H. Bennett, V. Provenzano, R. D. Shull, I. Levin, E. Della Torre, Y. Jin, *J. Alloys Comp.* **2012**, *525*, 34.
[35] R. Kainuma, Y. Imano, W. Ito, Y. Sutou, H. Morito, S. Okamoto, O. Kitakami, K. Oikawa, A. Fujita, T. Kanomata, K. Ishida, *Nature* **2006**, *439*, 957.
[36] K. Ullakko, J. K. Huang, C. Kantner, R. C. O'Handley, *Appl. Phys. Lett.* **1996**, *69*, 1966.
[37] A. Planes, T. Castán, A. Saxena, *Phil. Mag.* **2014**, *94*, 1893.
[38] P. Lloveras, G. Touchagues, T. Castán, T. Lookman, M. Porta, A. Saxena, A. Planes, *Phys. Stat. Sol. B* **2014**, *251*, 2080.
[39] J. F. Gebbia, P. Lloveras, T. Castán, A. Saxena, A. Planes, *Shape Mem. Superel.* **2015**, *1*, 347.
[40] Z. Zhao, X. Ding, J. Sun, E. K. H. Salje, *J. Phys. Cond. Matt.* **2014**, *26*, 142201.
[41] M. Porta, T. Castán, P. Lloveras, T. Lookman, A. Saxena, S. R. Shenoy, *Phys. Rev. B* **2009**, *79*, 214117.
[42] A. N. Vasilev, A. D. Bozhko, V. V. Khovailo, I. E. Dikshtein, V. G. Shavrov, V. D. Buchelnikov, M. Matsumoto, S. Suzuki, T. Takagi, J. Tani, *Phys. Rev. B* **1999**, *59*, 1113.
[43] P. Lloveras, T. Castán, M. Porta, A. Planes, A. Saxena, *Phys. Rev. Lett.* **2008**, *100*, 165707.
[44] A. Morrish, *The Physical Principles of Magnetism*. Wiley, New York, USA **1995**.
[45] J. Zhang, L. Chen, *Acta Mater.* **2005**, *53*, 2845.
[46] C. Kittel, *Rev. Mod. Phys.* **1949**, *21*, 541.
[47] R. Tickle, R. D. James, *J. Magn. Magn. Mater.* **1999**, *195*, 627.
[48] S. R. Shenoy, T. Lookman, A. Saxena, A. R. Bishop, *Phys. Rev. B* **1999**, *60*, R12537.
[49] F. J. Pérez-Reche, E. Vives, L. Mañosa, A. Planes, *Phys. Rev. Lett.* **2001**, *87*, 195701.
[50] F. Xiao, T. Fukuda, T. Kakeshita, *Phil. Mag.* **2015**, *95*, 1390.
[51] F. Lambrecht, N. Sagardiluz, M. Gueltig, I. R. Aseguinolaza, V. A. Chernenko, M. Kohl, *Appl. Phys. Lett.* **2017**, *110*, 213104.
[52] R. Niemann, O. Heczko, L. Schultz, S. Fähler, *Int. J. Refrig.* **2014**, *37*, 281.
[53] E. Bonnot, R. Romero, L. Mañosa, E. Vives, A. Planes, *Phys. Rev. Lett.* **2008**, *100*, 125901.

[54] P. Lloveras, T. Castán, M. Porta, A. Planes, A. Saxena, *Phys. Rev. B* **2010**, *81*, 214105.
[55] J. Marcos, L. Mañosa, A. Planes, F. Casanova, X. Batlle, A. Labarta, *Phys. Rev. B* **2003**, *68*, 094401.
[56] J. N. Armstrong, M. R. Sullivan, M. Romancer, V. A. Chernenko, M. D. Chopra, *J. Appl. Phys*. **2008**, *103*, 023905.
[57] Y. W. Lai, N. Scheerbaum, D. Hinz, O. Gutfleisch, R. Schäfer, L. Schultz, J. McCord, *Appl. Phys. Lett*. **2007**, *90*, 192504.
[58] P. J. Webster, K. R. A. Ziebeck, S. L. Town, M. S. Peak, *Phil. Mag*. **1984**, *49*, 295.
[59] J. Worgull, E. Petti, J. Trivisonno, *Phys. Rev. B* **1996**, *54*, 15965.
[60] L. Mañosa, A. Gonzàlez-Comas, E. Obradó, A. Planes, V. A. Chernenko, V. V. Kokorin, E. Cesari, *Phys. Rev. B* **1997**, *55*, 11068.
[61] S. Wirth, A. Leithe-Jasper, A. N. Vasilev, J. M. D. Coey, *J. Magn. Magn. Mater.* **1997**, *167*, L7.
[62] S. J. Murray, M. Marioni, S. M. Allen, R. C. O'Handley, T. A. Lograsso, *Appl. Phys. Lett*. **2000**, *77*, 886.
[63] N. Glavatska, G. Mogilniy, I. Glavatsky, S. Danilkin, D. Hohlwein, A. Beskrovnij, O. Söderberg, V. K. Lindroos, *J. Phys. IV* **2003**, *112*, 963.
[64] P. P. Wu, X. Q. Ma, J. X. Zhang, L. Q. Chen, *XXX*[Q10] **2008**, *104*, 073906.
[65] V. V. Khovaylo, V. D. Buchelnikov, R. Kainuma, V. V. Koledov, M. Ohtsuka, V. G. Shavrov, T. Takagi, S. V. Taskaev, A. N. Vasiliev, *Phys. Rev. B* **2005**, *72*, 224408.
[66] S. Ozdemir Kart, T. Cagin, *J. Alloys Compd*. **2010**, *508*, 177.
[67] D. I. Paul, J. Marquiss, Quattrochi[Q11], *J. Appl. Phys*. **2003**, *93*, 4561.
[68] T. Koyama, H. Onodera, *Mater. Trans*. **2003**, *44*, 2503.
[69] C. Mennerich, F. Wendler, M. Jainta, B. Nestler, *Arc. Mech*. **2011**, *63*, 549.
[70] S. Kartha, J. A. Krumhansl, J. P. Sethna, L. K. Wickham, *Phys. Rev. B* **1995**, *52*, 803.

